Temperature-induced magnonic Chern insulator in collinear antiferromagnets

Yun-Mei Li,[1,*] Xi-Wang Luo,[2] and Kai Chang[3]
[1]Department of Physics, School of Physical Science and Technology, Xiamen University, Xiamen 361005, China
[2]CAS Key Laboratory of Quantum Information, University of Science and Technology of China, Hefei 230026, China
[3]SKLSM, Institute of Semiconductors, Chinese Academy of Sciences, P.O. Box 912, Beijing 100083, China

(Received 6 October 2022; revised 30 May 2023; accepted 2 June 2023; published 13 June 2023)

Thermal fluctuation in magnets causes temperature-dependent self-energy corrections in magnons; however, its effects on the topological orders of magnons is not well explored. Here we demonstrate that such corrections can induce a Chern insulating phase in two-dimensional collinear antiferromagnets with sublattice asymmetries by increasing temperature. We present the phase diagram of the system and show that the trivial magnon bands at zero temperature exhibit Chern insulating phase above a critical temperature before the paramagnetic phase transition. The self-energy corrections close and reopen the band gap at Γ or **K** points, accompanied by a magnon chirality switch and nontrivial Berry curvature transition. The thermal Hall effect of magnons or detecting the magnon polarization can highlight the experimentally prominent signatures of the topological transitions. We include the numerical results based on the van der Waals magnet $MnPS_3$, calling for experimental implementation. Our work presents a paradigm for constructing topological phases that is beyond the linear spin wave theory.

DOI: 10.1103/PhysRevB.107.214417

I. INTRODUCTION

The last 20 years have witnessed the extraordinary development of topological insulators and semimetals in the field of condensed matter physics [1–14]. In analogy to electronic systems, the topological phases have also been extended to bosonic systems, such as photonic [15] and acoustic systems [16]. Magnons, quantized spin excitations in magnets, another boson, have also been proposed to host nontrivial topological phases, realized in magnets with artificially designed structures [17–19], special crystal symmetries [20–28], or quantum fluctuations [29]. The emergence of edge or surface states immune to disorder and back scattering has great potential for designing magnonic devices [30,31] with low dissipation and power consumption.

One of the key features in magnetic systems is the presence of magnon-magnon interactions (MMIs) and thermal fluctuation. Their interplay would give rise to temperature-dependent nonlinear self-energy corrections to the magnons [32–39]. Recently, two works [28,29] stated that nonlinear corrections can drive a topological phase transition of Dirac magnons hosting opposite Chern numbers at a critical temperature. Other works discussed the magnon topology within the linear spin wave theory [17–27,40] or only the magnon renormalization effect [35–39]. None of them addressed the possibilities of realizing topological phases of magnons above a finite temperature T_c while the bands below T_c are topologically trivial, with T_c being below the Curie or Néel temperature. This is quite reasonable because the specific schemes responsible for the topological phases at zero temperature are always present or absent in the self-energies at finite temperatures. This picture explains why few works have explored the construction of a topological phase at finite temperatures.

In this paper, we show that increasing temperature can actually induce a topological phase for magnons by considering the two-dimensional collinear antiferromagnet $MnPS_3$ as an example. We introduce sublattice asymmetric magnetic interactions induced in heterostructures, breaking the $\mathcal{PT}$ symmetry and magnon band degeneracies. We find that at zero temperature, the Chern insulating phase emerges but exists in only a finite interval of the single-ion easy-axis anisotropy strength. The self-energy corrections do not destroy this topological phase. Outside the interval, the magnon bands are topologically trivial at $T = 0$. But as temperature increases, due to the self-energies, the band gap at Γ or **K** points will be closed and reopen above a critical temperature T_c, which is well below the Néel temperature. The topological invariant, i.e., the Chern integer of the acoustic branch, changes from 0 to 1 across T_c. We also find that the band gap closing and reopening are accompanied by a magnon chirality switch and nontrivial Berry curvature transition near Γ or **K** points. The thermal Hall effect of magnons provides a prominent signature of the topological phase transitions near the Γ point. Detecting the magnon polarization also provides other experimental proof. Our proposal and conclusion are quite universal for collinear antiferromagnets and can be extended to ferrimagnets.

This paper is organized as follows. In Sec. II, we present the model and use the finite-temperature field theory to deal with the MMIs. In Sec. III, we calculate the magnon bands at both zero and finite temperatures and the corresponding topological invariant. We present the phase diagram and discuss the topological phase induced by the increasing temperature.

*Corresponding author: yunmeili@xmu.edu.cn

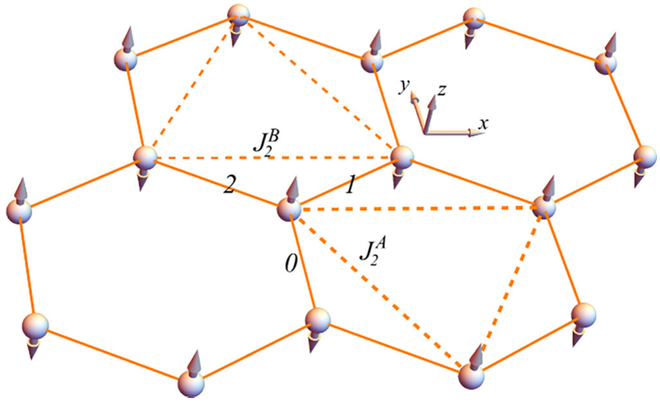

FIG. 1. Illustration of the honeycomb antiferromagnet with sublattice asymmetry. The numbers denote the bond index. Spins on the A sublattice point up, while those on the B sublattice point down. The intrasublattice second-neighbor interactions on the two sublattices are denoted as J_2^A and J_2^B, respectively.

We also discuss the thermal Hall effect of magnons and the chirality switch during the topological phase transitions, which can be probed in realistic experiments. Finally, we summarize in Sec. IV.

II. MODEL AND METHODOLOGY

We consider a honeycomb collinear antiferromagnet, as illustrated in Fig. 1. The spin interaction Hamiltonian is given by

$$H = J_1 \sum_{\langle ij \rangle} \mathbf{S}_i \cdot \mathbf{S}_j + I_1 \sum_{\langle ij \rangle} S_i^z S_j^z + \sum_{\langle\langle ij \rangle\rangle} J_2^{ij} \mathbf{S}_i \cdot \mathbf{S}_j + \frac{J_a}{2} \sum_{\langle ij \rangle} (\gamma_{ij} S_i^+ S_j^+ + \gamma_{ij}^* S_i^- S_j^-) - \sum_i K_i (S_i^z)^2. \quad (1)$$

The first and second terms denote the Heisenberg exchange interaction between nearest neighbors with an Ising-type exchange anisotropy characterized by I_1. The third term denotes the Heisenberg exchange interaction between second neighbors, describing the interaction between spins in the same A or B sublattice (Fig. 1), characterized by J_2^A and J_2^B, respectively. Here we assume $J_2^A \neq J_2^B$. The fourth term is the bond-dependent interactions [41] between nearest neighbors, allowed by the symmetry and consistent with recent experiments with $MnPS_3$ [42]. $\gamma_{ij} = e^{i2\pi n/3}$, with $n = 0, 1, 2$ being the bond index, as illustrated in Fig. 1. The last term is the sublattice asymmetric single-ion easy-axis anisotropy, characterized by K_A and K_B for the two sublattices. The Hamiltonian with $J_2^A = J_2^B$ and without K_A and K_B was proposed for $MnPS_3$ [41]. The exchange anisotropy I_1, the difference between J_2^A and J_2^B, and the anisotropy fields K_A and K_B can be induced or tuned in the $MnPS_3$ homobilayer or in the $MnPS_3/CrCl_3$ heterostructure, verified by very recent first-principles calculations [43,44]. For negative and quite small positive J_2^A and J_2^B, the ground state stays in the collinear antiferromagnetic phase [45,46].

We apply the Holstein-Primakoff transformation, $S^z = S - a^\dagger a$, $S^+ = \sqrt{2S - a^\dagger a}\, a$, and $S^- = a^\dagger \sqrt{2S - a^\dagger a}$ for the A sublattice and $S^z = -S + b^\dagger b$, $S^+ = b^\dagger \sqrt{2S - b^\dagger b}$, and $S^- = \sqrt{2S - b^\dagger b}\, b$ for the B sublattice. The Hamiltonian in Eq. (1) can be expanded as $H = \sum_{p=0}^{\infty} H_{2p}$, where $2p$ denote the number of bosonic operators. We here keep the terms up to quartic order and neglect the ground state energy term. With a Fourier transformation, the two-particle term can be written in the form $H_2 = \frac{1}{2} \sum_{\mathbf{k}} \Psi_k^\dagger H_{\mathbf{k}} \Psi_k$, where $\Psi_k = (a_{\mathbf{k}}, b_{\mathbf{k}}, a_{-\mathbf{k}}^\dagger, b_{-\mathbf{k}}^\dagger)^T$; the uppercase T denotes the transpose. We have

$$H_{\mathbf{k}} = \begin{pmatrix} h_{\mathbf{k}} & \Delta_{\mathbf{k}} \\ \Delta_{\mathbf{k}}^\dagger & h_{-\mathbf{k}}^T \end{pmatrix}, \quad (2)$$

where $h_{\mathbf{k}} = h_0 \mathbb{I}_2 + \mathbf{h} \cdot \boldsymbol{\sigma}$ and $\Delta_{\mathbf{k}} = \boldsymbol{\delta} \cdot \boldsymbol{\sigma}$. $\boldsymbol{\sigma}$ denotes the sublattice index, with $h_0 = (h_A + h_B)/2$, $h_x = J_a S \mathrm{Re}(g_{\mathbf{k}})$, $h_y = -J_a S \mathrm{Im}(g_{\mathbf{k}})$, $h_z = (h_A - h_B)/2$, $\delta_x = J_1 S \mathrm{Re}(f_{\mathbf{k}})$, $\delta_y = -J_1 S \mathrm{Im}(f_{\mathbf{k}})$, $h_A = K_A(2S-1) + 3(J_1 + I_1)S - J_2^A S(6 - d_{\mathbf{k}})$, $h_B = K_B(2S-1) + 3(J_1 + I_1)S - J_2^B S(6 - d_{\mathbf{k}})$, $g_{\mathbf{k}} = 1 + 2e^{i\frac{3}{2}k_y} \cos(\frac{\sqrt{3}}{2}k_x + \frac{2\pi}{3})$, $f_{\mathbf{k}} = 1 + 2e^{i\frac{3}{2}k_y} \cos(\frac{\sqrt{3}}{2}k_x)$, $d_{\mathbf{k}} = \sum_{i=1}^{6} \cos(\mathbf{k} \cdot \mathbf{a}_i)$, and $\mathbf{a}_i$ are the second-neighbor lattice vectors. Notice that $g_{\mathbf{k}}^* \neq g_{-\mathbf{k}}$, indicating the broken time-reversal symmetry in our system, and we can use the Chern integer to characterize the topological properties of magnon bands.

We now discuss the effect of MMIs, i.e., the four-particle term H_4. We have

$$\begin{aligned} H_4 = -\frac{1}{N} \sum_{\{\mathbf{k}_i\}} \frac{J_1}{4} \big(& f_{\mathbf{k}_4} a_{\mathbf{k}_1}^\dagger a_{\mathbf{k}_2} a_{\mathbf{k}_3} b_{\mathbf{k}_4} + f_{\mathbf{k}_4}^* b_{\mathbf{k}_1}^\dagger b_{\mathbf{k}_2} b_{\mathbf{k}_3} a_{\mathbf{k}_4} \\ & + \mathrm{H.c.} \big) \delta_{\{\mathbf{k}_i\}}^1 + \big[(J_1 + I_1) f_{\mathbf{k}_4 - \mathbf{k}_2} a_{\mathbf{k}_1}^\dagger b_{\mathbf{k}_2}^\dagger a_{\mathbf{k}_3} b_{\mathbf{k}_4} \\ & + \frac{J_a}{4} \big(g_{\mathbf{k}_3} a_{\mathbf{k}_1}^\dagger a_{\mathbf{k}_2}^\dagger b_{\mathbf{k}_3} a_{\mathbf{k}_4} + g_{\mathbf{k}_1} a_{\mathbf{k}_1}^\dagger b_{\mathbf{k}_2}^\dagger b_{\mathbf{k}_3} b_{\mathbf{k}_4} + \mathrm{H.c.} \big) \\ & + \big(\epsilon_A a_{\mathbf{k}_1}^\dagger a_{\mathbf{k}_2}^\dagger a_{\mathbf{k}_3} a_{\mathbf{k}_4} + \epsilon_B b_{\mathbf{k}_1}^\dagger b_{\mathbf{k}_2}^\dagger b_{\mathbf{k}_3} b_{\mathbf{k}_4} \big) \big] \delta_{\{\mathbf{k}_i\}}^2, \end{aligned} \quad (3)$$

where $\delta_{\{\mathbf{k}_i\}}^1 = \delta_{\mathbf{k}_1, \mathbf{k}_2 + \mathbf{k}_3 + \mathbf{k}_4}$, $\delta_{\{\mathbf{k}_i\}}^2 = \delta_{\mathbf{k}_1 + \mathbf{k}_2, \mathbf{k}_3 + \mathbf{k}_4}$, $\epsilon_{A,B} = J_2^{A,B} d_{\{\mathbf{k}_i\}} + K_{A,B}$, and $d_{\{\mathbf{k}_i\}} = \frac{d_{\mathbf{k}_1} + d_{\mathbf{k}_4} - 2d_{\mathbf{k}_4 - \mathbf{k}_2}}{4}$. To consider the many-body effect and its interplay with thermal fluctuation, we employ the Green's function method and define a matrix Green's function as $\hat{G}(\mathbf{k}, \tau) = -\langle T_\tau \Psi_{\mathbf{k}}(\tau) \Psi_{\mathbf{k}}^\dagger(0) \rangle$ [47], where T_τ is the chronological operator for the imaginary time τ. The Heisenberg operator is defined as $A(\tau) = e^{\tau H} A(0) e^{-\tau H}$, and $H = H_2 + H_4$ is Hermitian. The bracket denotes the thermal average. To get the solution, we solve the Heisenberg equation of motion for the Green's function elements and apply the random phase approximation to extract the nonlinear self-energy corrections from MMIs. After a Fourier transformation $\hat{G}(\mathbf{k}, \tau) = (1/\beta) \sum_n \hat{G}(\mathbf{k}, \omega_n) e^{-i\omega_n \tau}$, with $\beta = 1/T$, where T is the temperature and ω_n is the bosonic Matsubara frequency, we can get the Dyson's equation $\hat{G}^{-1}(\mathbf{k}, \omega_n) = i\omega_n \tau_z - H_{\mathbf{k}}^{\mathrm{eff}}$ and the effective Hamiltonian

$$H_{\mathbf{k}}^{\mathrm{eff}} = H_{\mathbf{k}} + \Sigma_{\mathbf{k}} = \begin{pmatrix} h_{\mathbf{k}}^{\mathrm{eff}} & \Delta_{\mathbf{k}}^{\mathrm{eff}} \\ (\Delta_{\mathbf{k}}^{\mathrm{eff}})^\dagger & (h_{-\mathbf{k}}^{\mathrm{eff}})^T \end{pmatrix}, \quad (4)$$

with $h_{\mathbf{k}}^{\mathrm{eff}} = h_0^{\mathrm{eff}} \mathbb{I}_2 + \mathbf{h}^{\mathrm{eff}} \cdot \boldsymbol{\sigma}$. $h_0^{\mathrm{eff}} = (h_A^{\mathrm{eff}} + h_B^{\mathrm{eff}})/2$, $h_x^{\mathrm{eff}} = J_a \frac{(\bar{S}_A + \bar{S}_B)}{2} \mathrm{Re}(g_{\mathbf{k}})$, $h_y^{\mathrm{eff}} = -J_a \frac{(\bar{S}_A + \bar{S}_B)}{2} \mathrm{Im}(g_{\mathbf{k}})$, $h_z = (h_A^{\mathrm{eff}} - h_B^{\mathrm{eff}})/2$, where $h_A^{\mathrm{eff}} = K_A(-2S - 1 + 4\bar{S}_A) + 3(J_1 + I_1)\bar{S}_B - J_2^A \bar{S}_A'(6 - d_{\mathbf{k}}) - h_A^r$, $h_B^{\mathrm{eff}} = K_B(-2S - 1 + 4\bar{S}_B) + 3(J_1 +$

$I_1)\bar{S}_A - J_2^B\bar{S}_B'(6-d_{\mathbf{k}}) - h_B^r$, $\bar{S}_A = S - \frac{1}{N}\sum_{\mathbf{q}}\langle a_{\mathbf{q}}^\dagger a_{\mathbf{q}}\rangle$, $\bar{S}_B = S - \frac{1}{N}\sum_{\mathbf{q}}\langle b_{\mathbf{q}}^\dagger b_{\mathbf{q}}\rangle$, $\bar{S}_A' = S + \frac{1}{6N}\sum_{\mathbf{q}} d_{\mathbf{q}}\langle a_{\mathbf{q}}^\dagger a_{\mathbf{q}}\rangle - \frac{1}{N}\sum_{\mathbf{q}}\langle a_{\mathbf{q}}^\dagger a_{\mathbf{q}}\rangle$, $\bar{S}_B' = S + \frac{1}{6N}\sum_{\mathbf{q}} d_{\mathbf{q}}\langle b_{\mathbf{q}}^\dagger b_{\mathbf{q}}\rangle - \frac{1}{N}\sum_{\mathbf{q}}\langle b_{\mathbf{q}}^\dagger b_{\mathbf{q}}\rangle$, $h_A^r = h_B^r = \frac{J_1}{N}\mathrm{Re}\sum_{\mathbf{q}} f_{\mathbf{q}}\langle a_{\mathbf{q}}^\dagger b_{-\mathbf{q}}^\dagger\rangle + \frac{J_a}{N}\mathrm{Re}\sum_{\mathbf{q}} g_{\mathbf{q}}\langle a_{\mathbf{q}}^\dagger b_{\mathbf{q}}\rangle$, $(\Delta_{\mathbf{k}}^{\mathrm{eff}})_{12} = \frac{(\bar{S}_A+\bar{S}_B)}{2}J_1 f_{\mathbf{k}} - \frac{J_1+I_1}{N}\sum_{\mathbf{q}} f_{\mathbf{k}-\mathbf{q}}\langle a_{\mathbf{q}} b_{-\mathbf{q}}\rangle$, and $(\Delta_{\mathbf{k}}^{\mathrm{eff}})_{21} = (\Delta_{-\mathbf{k}}^{\mathrm{eff}})_{12}$. The other terms in the random phase approximation always vanish and are thus neglected. By diagonalizing the effective Hamiltonian in Eq. (4), $\Lambda_{\mathbf{k}}^\dagger H_{\mathbf{k}}^{\mathrm{eff}}\Lambda_{\mathbf{k}} = \mathrm{diag}\{E_{\mathbf{k}}, E_{-\mathbf{k}}\}$, we have $H_{\mathbf{k}}^{\mathrm{eff}} = \sum_{\mathbf{k}}(E_{\mathbf{k}}^\alpha \alpha_{\mathbf{k}}^\dagger\alpha_{\mathbf{k}} + E_{\mathbf{k}}^\beta \beta_{\mathbf{k}}^\dagger\beta_{\mathbf{k}})$ up to a zero-point energy. The paraunitary eigenvectors satisfy $\Lambda_{\mathbf{k}}^\dagger\tau_z\Lambda_{\mathbf{k}} = \tau_z$, and τ_z is the Pauli matrix acting on the particle-hole space [17]. Note that the diagonalization gives us the relation $\Psi_{\mathbf{k}} = \Lambda_{\mathbf{k}}\Phi_{\mathbf{k}}$, with $\Phi_{\mathbf{k}} = (\alpha_{\mathbf{k}}, \beta_{\mathbf{k}}, \alpha_{-\mathbf{k}}^\dagger, \beta_{-\mathbf{k}}^\dagger)^T$.

The additional term in Eq. (4) compared to Eq. (2) is the self-energy matrix term $\Sigma_{\mathbf{k}}$. Using the relation $\Psi_{\mathbf{k}} = \Lambda_{\mathbf{k}}\Phi_{\mathbf{k}}$, the element of the self-energy matrix can be expressed as

$$\Sigma_{\mathbf{k}}^{ij} = \frac{1}{N}\sum_{\mathbf{q},\lambda=\alpha,\beta}\left[T_{ij}^\lambda(\mathbf{k},\mathbf{q})n_{\mathbf{q},\lambda}(T) + Q_{ij}^\lambda(\mathbf{k},\mathbf{q})\right], \quad (5)$$

where $n_{\mathbf{q},\lambda}$ is the Bose-Einstein distribution function $n_{\mathbf{q},\lambda} = (e^{E_{\mathbf{q}}^\lambda/T} - 1)^{-1}$ with a zero chemical potential. The right two terms in Eq. (5) correspond to the thermal and quantum corrections, respectively. The method to calculate them is presented in Appendix A. Notice that the self-energy corrections do not vanish even at zero temperature due to the quantum fluctuations. Like in previous works [38,39], Eqs. (4) and (5) and the diagonalization relation above form the self-consistent relations. We can calculate the band structures at given temperatures self-consistently and obtain corresponding Chern integers. The results for temperature-induced topological phases are presented below.

III. RESULTS AND DISCUSSION

A. Phase diagram and topological transitions

We first discuss the topological phase at zero temperature $T = 0$ to get an intuitive picture of the system. The two magnon bands are usually degenerate in pristine antiferromagnets. The sublattice asymmetric second-neighbor exchange interaction and sublattice asymmetric single-ion easy-axis anisotropy break the band degeneracy. Especially, for $J_2^A \neq J_2^B$, the two magnon bands have different group velocities at the same energies even when $K_A = K_B$. That is to say, the two magnon bands will separate totally or show degeneracy at limited momenta. We find that when $J_a = 0$ and $J_2^A > J_2^B$, in the region $0 < K_A - K_B < K_c$, the two magnon bands will show a ringlike band intersection, as shown in Fig. 2(a) by the solid lines. Here $K_c \simeq 9(J_2^A - J_2^B)\bar{S}'/(4\bar{S} - 2S - 1)$, with $\bar{S} = \bar{S}_A = \bar{S}_B$ and $\bar{S}' = \bar{S}_A' = \bar{S}_B'$ at zero temperature. Here we have considered the quantum corrections. At $K_A = K_B$ ($K_A = K_B + K_c$), the two bands show point touching at the Γ ($\mathbf{K}$ and $\mathbf{K}'$) point(s) in the Brillouin zone (BZ). Outside the above interval, the two bands are always separated and topologically trivial even for $J_a \neq 0$.

Finite J_a is expected to gap the two bands and lead to nontrivial topology when $0 < K_A - K_B < K_c$. As $g_{\mathbf{k}}$ vanishes at the Γ and $\mathbf{K}$ points; the band point touching at the Γ ($\mathbf{K}$) point when $K_A = K_B$ ($K_A = K_B + K_c$) will not be changed. Thus, the

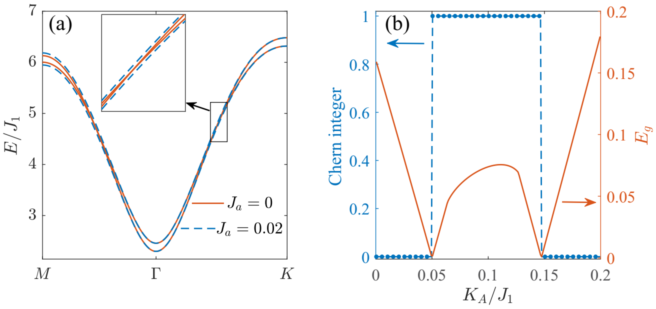

FIG. 2. (a) The magnon band structures at $T = 0$ and $K_A = 0.1$. The other parameters are adopted as $S = 2.5$, $J_1 = 1.0$, $I_1 = 0.05$, $J_2^A = 0.08$, $J_2^B = 0.065$, and $K_B = 0.05$. All the parameters are in units of $J_1 = 1.54$ meV. In subsequent calculations, we adopt the same parameters when not stated otherwise. $J_a = 0$ for the solid line, and $J_a = 0.02$ for the dashed lines. (b) The Chern integer for the acoustic branch and band gap with respect to K_A at $T = 0$. The other parameters are the same as in (a) with $J_a = 0.02$. The band gap is defined as $E_g = \min_{\mathbf{k}}(E_{\mathbf{k}}^\beta - E_{\mathbf{k}}^\alpha)$ along the Γ-$\mathbf{K}$ direction.

two conditions give the phase boundaries between trivial and nontrivial topological phases. In Fig. 2(a), we can see that the two bands are gapped in the intersection region (dashed lines). Figure 2(b) gives the gap evolution along the Γ-$\mathbf{K}$ direction. We use the Chern integer as the topological invariant, defined as $C_\lambda = \frac{1}{2\pi}\int_{\mathrm{BZ}} B_\lambda^z d^2\mathbf{k}$, with Berry curvature $\mathbf{B}_\lambda = \nabla \times \mathbf{A}_\lambda$ and Berry connection $\mathbf{A}_\lambda = i\mathrm{Tr}[\Gamma^\lambda\Lambda_{\mathbf{k}}^\dagger\tau_z(\partial_{\mathbf{k}}\Lambda_{\mathbf{k}})]$, where Γ^λ is the diagonal matrix, taking a value of $+1$ for the λ mode and zero otherwise. We find the Chern integer is 1 inside the interval $K_B < K_A < K_B + K_c$ for the acoustic branch, as presented in Fig. 2(b). When the sublattice asymmetric second-neighbor exchange interaction is reversed, i.e., $J_2^A < J_2^B$, the nontrivial topological phase lies in the interval $0 < K_B - K_A < K_c'$, and the Chern integer for the acoustic branch is -1, with $K_c' \simeq 9(J_2^B - J_2^A)\bar{S}'/(4\bar{S} - 2S - 1)$. In the subsequent discussion, we will focus on $J_2^A > J_2^B$ because the two cases share the same physics.

We now consider the effect of nonlinear self-energy corrections at finite temperatures and show that the trivial bands at $T = 0$ will also exhibit the Chern insulating phase above a critical temperature before the paramagnetic phase transition. We first present the phase diagram directly and choose the Chern integer of the acoustic branch as the order parameter, calculated from the effective Hamiltonian after self-consistent treatment at given temperatures. The definition of the Chern integer is the same as in the paragraph above by adopting the eigenvectors of the isolated magnon bands at finite temperatures. Therefore, the Chern integer is still quantized. Here the temperature can change the topological properties of the magnon bands via the temperature-dependent self-energies in Eq. (5) due to the MMIs. The self-consistent process also helps us to confirm that the temperatures we choose are all below the Néel temperature T_N. The phase diagram in the K_A-T plane is shown in Fig. 3(a). We can see that when $K_B < K_A < K_B + K_c$, the topological phase will not be destroyed by the nonlinear corrections, the same as in previous works. Interestingly, when $K_A < K_B$ and $K_A > K_B + K_c$, the magnon bands show a trivial phase at low temperatures but

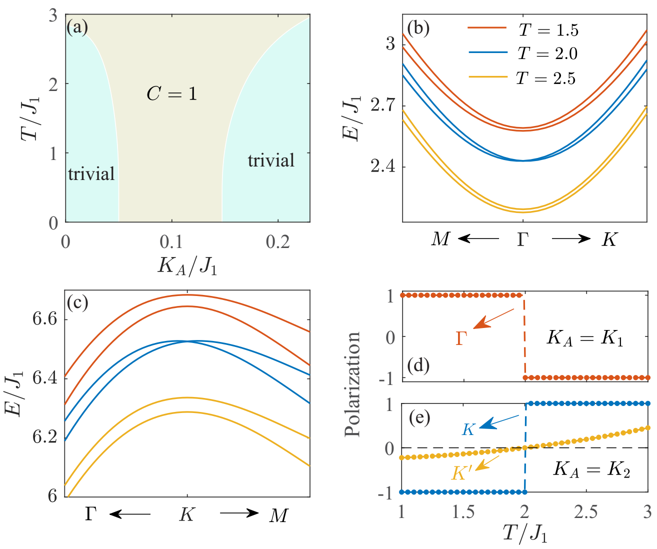

FIG. 3. (a) The phase diagram in the K_A-T plane. The Chern number is for the acoustic branch, and the Chern number for the optical branch is the opposite. The temperature unit is $T_0 = J_1/k_B \simeq 17.9$ K, with $J_1 = 1.54$ meV. (b) Magnon bands near the Γ point at three temperatures. $K_A = K_1 = 0.041$. (c) Magnon bands near the K point at the same three temperatures as in (b). $K_A = K_2 = 0.169$. At K_1 and K_2, the critical temperature of the topological transition is almost the same, $T_c/J_1 \simeq 2$. (d) The magnon chirality switch at the Γ point for $K_A = K_1$. (e) The magnon chirality switch at the K point and DOP evolution at the K' point for $K_A = K_2$. For all the plots, $J_a = 0.02$.

exhibit a Chern insulating phase above a critical temperature T_c, which is dependent on K_A. Note that here T_c is below the Néel temperature T_N. This phenomenon is quite surprising and is not presented or discussed in the previous works on topological phase of magnons. This indicates that the thermal fluctuation can, indeed, induce a magnonic topological insulating phase when we consider the nonlinear effect from MMIs. Note that the temperature-induced phase transition is similar to that of the topological Anderson insulator induced by disorder [48–51], in the sense that the topology is induced by fluctuation (either thermal or parametric).

To further investigate these thermal fluctuation induced topological transitions at finite temperatures, we plot the magnon bands at three temperatures for $K_A \simeq 0.041(K_1) < K_B$ and $K_A \simeq 0.169(K_2) > K_B + K_c$ in Figs. 3(b) and 3(c), respectively. The critical temperature of topological transition for the two values are almost the same, $T_c/J_1 \simeq 2$. For $K_a = K_1$, we plot the bands near the Γ point. Besides the magnon energy renormalization, we can see the band gap at the Γ point decreases as the temperature increases. The spectrum become gapless at $T = T_c$. Further increasing the temperature reopens the gap. During this process, we have checked that the two bands at other points in the BZ are always gapped. From the phase diagram in Fig. 3(a), the Chern integer is 0 below T_c and 1 above T_c. The other $K_A < K_B$ values have the same behavior with different critical temperatures T_c. Such a temperature-induced topological phase in the region $K_A < K_B$ is related to the weak ferrimagnetic phase induced at finite temperatures (see Appendix B), arising from the imbalanced occupation number of the two magnon branches. The zero band gap condition at the Γ point is $K_A(-2S - 1 + 4\bar{S}_A) + 3(J_1 + I_1)\bar{S}_B = K_B(-2S - 1 + 4\bar{S}_B) + 3(J_1 + I_1)\bar{S}_A$. $\bar{S}_A \neq \bar{S}_B$ at finite temperatures requires $K_A < K_B$ for the topological transition in this case. This temperature-induced topological transition is totally due to the thermal fluctuation. That is to say, when $K_a = K_b$, a weak perpendicular magnetic field can replace the role of easy-axis asymmetry to get the same results with a negative magnetic field. The phase diagram is presented in Appendix C. For $K_A = K_2$, the magnon bands experience a similar behavior, but the gap closes and reopens at the $\mathbf{K}$ point instead, as shown in Fig. 3(c). For both cases, the thermal fluctuation induces gap closing and reopening, and the topological invariant, i.e., the Chern integer, jumps from 0 to 1. In experiments, the band gap closing and reopening can be detected by neutron resonance spin echo spectroscopy [42], which can detect the band gap down to the limit of μeV.

B. Magnon chirality switch

The Néel vectors of two magnon modes precess circularly with opposite chiralities when $J_a = 0$ [52]. For finite J_a, the precession trajectories will become elliptical. The polarization of the magnons in the antiferromagnet is similar to that of light. We can define the degree of polarization (DOP) for magnons in momentum space. At a given $\mathbf{k}$, the eigenvector at finite J_a can be expressed as a linear combination of the polarized state at $J_a = 0$, so we have $\Lambda_{\mathbf{k}}^{\lambda} = \chi_{\mathbf{k},\lambda}^{+}\Lambda_{\mathbf{k}}^{+} + \chi_{\mathbf{k},\lambda}^{-}\Lambda_{\mathbf{k}}^{-}$ ($\lambda = \alpha, \beta$), where $\Lambda_{\mathbf{k}}^{\pm}$ are the eigenvectors for right- and left-handed precession modes when $J_a = 0$ and $\chi_{\mathbf{k},\lambda}^{\pm}$ are the expansion coefficients and satisfy $|\chi_{\mathbf{k},\lambda}^{+}|^2 + |\chi_{\mathbf{k},\lambda}^{-}|^2 = 1$. The DOP in momentum space is defined as $\mathcal{P}(\mathbf{k}) = |\chi_{\mathbf{k},\lambda}^{+}|^2 - |\chi_{\mathbf{k},\lambda}^{-}|^2$. Below we will focus on only the acoustic branch, and the DOP for the optical branch is the opposite. At zero temperature and $J_a = 0$, the chirality is right-handed for $K_A < K_B$ [$\mathcal{P}(\mathbf{k}) = 1$] and left-handed for $K_A > K_B + K_c$ [$\mathcal{P}(\mathbf{k}) = -1$]. Finite J_a does not break the chirality at the $\mathbf{K}$ and Γ points. Therefore, the chirality at the $\mathbf{K}$ and Γ points in the left trivial region in the phase diagram in Fig. 3(a) is right-handed, while in the right trivial region it is left-handed. In the middle topologically nontrivial region, we find the chirality is right-handed at the $\mathbf{K}$ point, while it is left-handed at the Γ point. These features indicate that the topological transitions are accompanied by a magnon chirality switch where the gap closes and reopens. When $K_A < K_B$, the chirality will be switched from right-handed to left-handed across T_c, as shown in Fig. 3(d). On the other side, $K_A > K_B + K_c$, the chirality will be switched from left-handed to right-handed, as shown in Fig. 3(e). Near the $\mathbf{K}'$ point, the magnon will also experience a chirality switch, the same as the $\mathbf{K}$ point when $J_a = 0$ and $K_A > K_B + K_c$. For finite J_a, the evolution of the DOP at $\mathbf{K}'$ shows a negative to positive transition [see Fig. 3(e)]. As reported in the experimental works [53–57], the magnon polarization in antiferromagnets can be detected by magneto-Raman spectroscopy [53], the polarized neutron scattering technique [54], or polarization-selective spectroscopy [55–57]. These experimental methods greatly coincide with our system. The detection of magnon polarization provides experimental proof of the temperature-induced topological transitions.

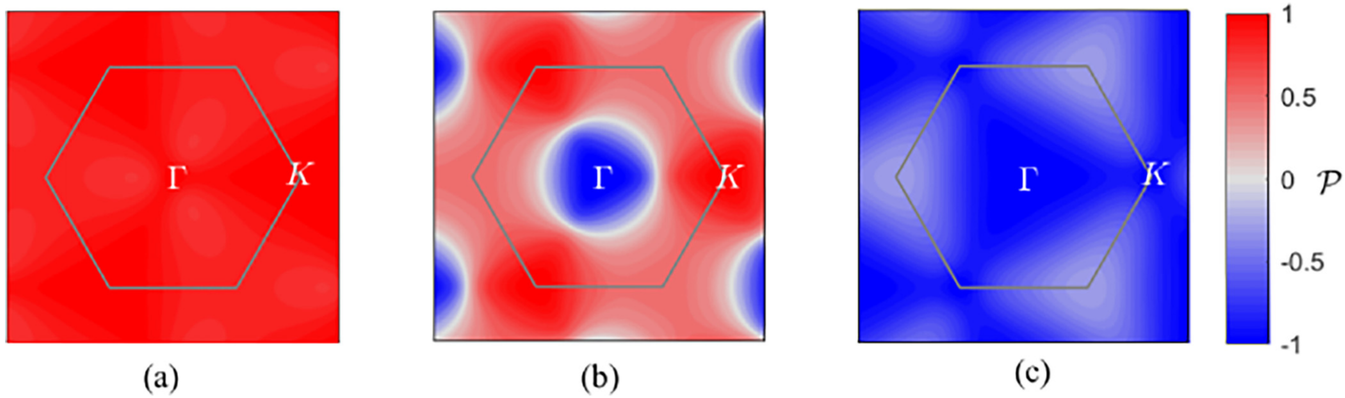

FIG. 4. The DOP distribution in the BZ in the three regions of the phase diagram in Fig. 3(a) for the acoustic branch. We adopt $K_A = 0.02$ in (a), 0.1 in (b), and 0.18 in (c). The temperature is set to $T = 1.5$.

We briefly discuss the DOP in the full BZ. There are three different regions in the phase diagram in Fig. 3(a). The typical DOP distributions in the BZ for the three regions are shown in Figs. 4(a)–4(c). In the left region, the DOP is positive [Fig. 4(a)], and the right-handed mode dominates. However, in the right region, the DOP is negative [Fig. 4(c)], and the left-handed mode dominates. In the middle topological region, $\mathcal{P}$ is negative near the Γ point and positive around the $\mathbf{K}$ point [Fig. 4(b)]. The ringlike transition zone where $\mathcal{P} \simeq 0$ is the band intersection region when $J_a = 0$. The differences indicate that the temperature will change the distribution, the detection of which using the experimental techniques above provides alternative experimental proof of our theory.

C. Thermal Hall effect

The topological transitions from trivial to nontrivial phases indicate nontrivial transitions of the Berry curvature distribution in momentum space. Therefore, the topological transitions of magnons are expected to manifest themselves in the thermal transport properties [58,59]. The thermal Hall conductivity is given by

$$\kappa_{xy} = -\frac{k_B^2 T}{\hbar} \sum_{\lambda=\alpha,\beta} \int [d\mathbf{k}] B_\lambda^z(\mathbf{k}) c_2(n_{\mathbf{k},\lambda}), \tag{6}$$

where $[d\mathbf{k}] = d^2\mathbf{k}/(2\pi)^2$, k_B is the Boltzmann constant, $\hbar$ is the reduced Planck constant, $c_2(x) = (1+x)(\ln\frac{1+x}{x})^2 - (\ln x)^2 - 2\mathrm{Li}_2(-x)$, and $\mathrm{Li}_2(x)$ is the polylogarithm function. We plot the temperature-dependent thermal Hall conductivities κ_{xy} in Figs. 5(a) and 5(b) with different K_A for comparison. We also give the Berry curvature distribution for a typical K_A value at temperatures below and above T_c.

For $K_A < K_B$, we give κ_{xy} with four different values, corresponding to different T_c. We can see all the κ_{xy} show discontinuous behavior across T_c. This can be interpreted from the Berry curvature transition near the Γ point, as shown in Figs. 5(c) and 5(d). The gap closes and reopens at the Γ point, and the Berry curvature experiences a jump from negative to positive values near the Γ point. From Eq. (6), the thermal Hall conductivity is dependent on the Berry curvature distribution and the occupation number of the magnon bands. The discontinuous change in Berry curvature leads to the discontinuous behavior of κ_{xy} across T_c, the same as the behavior of the Chern integer, which is the integral of the Berry curvature. The discontinuity of κ_{xy} with respect to temperature is prominent and experimentally distinguishable. Therefore, the thermal Hall effect of magnons provides another route to probe the topological transition experimentally.

For $K_A > K_B + K_c$, we can see κ_{xy} with respect to the temperature do not show a discontinuity near T_c [Fig. 5(b)]. This is because the thermal Hall effect of magnons is mainly contributed by the magnons with low energies. The band gap closes and reopens at $\mathbf{K}$ points with energies quite large compared to $k_B T_c$. The nontrivial Berry curvature transition near the $\mathbf{K}$ point has a negligible effect on κ_{xy}. As the case $K_A < K_B$ is mostly experimentally approachable, the thermal

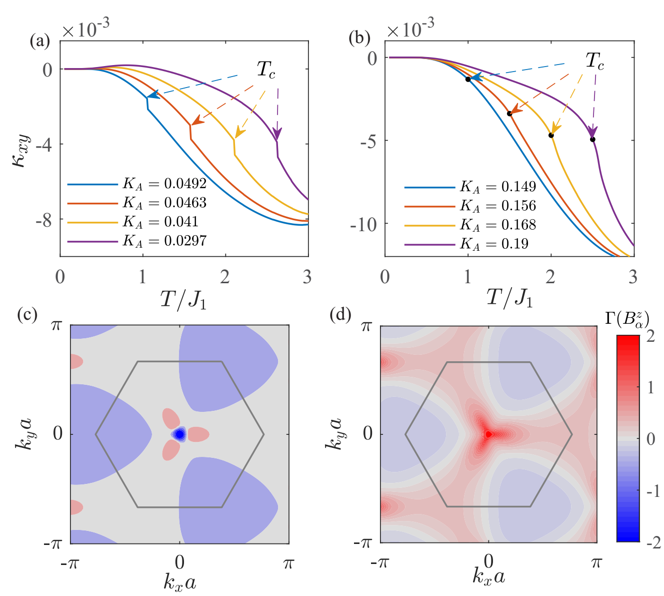

FIG. 5. (a) and (b) The thermal Hall conductivity of four different K_a values for $K_a < K_b$ and $K_a > K_c$, respectively. The corresponding critical temperature T_c is $T_c/J_1 = 1, 1.5, 2, 2.5$, respectively. κ_{xy} is in units of $k_B J_1/\hbar = 3.23 \times 10^{-11}$ W/K for $J_1 = 1.54$ meV. The distribution of Berry curvatures in log scale $\Gamma(B_\alpha^z) = \mathrm{sgn}(B_\alpha^z)\log(1 + |B_\alpha^z|)$ for (c) $T/J_1 = 1.8$ and (d) $T/J_1 = 2.2$ at $K_a = 0.041$. (c) and (d) share the color bar. The gray hexagon denotes the first Brillouin zone.

Hall effect can be an indicator of the topological transitions of magnons in realistic experiments.

D. Discussion

Above all, by challenging the belief in former works that thermal fluctuation cannot induce a nontrivial topological phase for magnons, we successfully build a Chern insulating phase above finite temperatures before the paramagnetic phase transition while the magnon bands at zero temperature are topologically trivial. The system is the collinear antiferromagnetic insulator $MnPS_3$ with sublattice asymmetries induced in a homobilayer or heterostructures. We also propose realistic schemes to detect these transitions experimentally. The role of the bond-dependent term can be replaced by the nearest-neighbor dipolar interactions (see Appendix D for the proof), which exist generally between the local spins in magnets. Recent neutron resonance spin echo spectroscopy verified the band splitting due to the dipolar interactions in $MnPS_3$ [42,60]. Meanwhile, the introduction of sublattice asymmetries in collinear antiferromagnets is independent of the lattice type. Therefore, our proposal and results should be universal for all two-dimensional collinear antiferromagnets with sublattice asymmetries and should not be limited to honeycomb lattices. Another van der Waals magnet, $MnPSe_3$ [61,62], is another promising candidate material. Since our proposal is based on broken sublattice symmetry, ferrimagnets [63], which lack it naturally, are expected to exhibit similar temperature-induced topological phase transitions.

IV. SUMMARY

In summary, we demonstrated that thermal fluctuation in magnets can induce nontrivial topological phases for magnons at finite temperature while at low temperature the bands are trivial. The transition between trivial and nontrivial topological phases can be probed with multiple state-of-the-art techniques by measuring the thermal Hall conductivity or detecting the magnon polarization. The temperature-dependent topological phase is quite important for designing topological devices at easily achievable higher temperatures. Our work paves the way for the study of the interplay between topological orders, MMIs, and thermal fluctuation that is beyond the linear spin wave theory.

ACKNOWLEDGMENTS

Y.-M.L. thanks Dr. Y.-J. Wu and Dr. B. Wei for helpful discussions. This work is supported by startup funding from Xiamen University. X.-W.L. acknowledges support from the National Natural Science Foundation of China (Grant No. 12275203) and the USTC startup funding.

APPENDIX A: THE EXPRESSIONS FOR THE SELF-ENERGIES

We here use the Green's function method and random phase approximation to get the nonlinear self-energy corrections. The Heisenberg equation of motion for the Green's function is given by

$$\frac{d\hat{G}(\mathbf{k},\tau)}{d\tau} = -\delta(\tau)\tau_z - \langle\mathcal{T}[H,\Psi_{\mathbf{k}}(\tau)]\Psi^\dagger_{\mathbf{k}}(0)\rangle$$
$$= -\delta(\tau)\tau_z - \tau_z(H_{\mathbf{k}}+\Sigma_{\mathbf{k}})\hat{G}(\mathbf{k},\tau).$$

Here the self-energy term $\Sigma_{\mathbf{k}}$ is from the random phase approximation. With the Fourier transformation $\hat{G}(\mathbf{k},\tau) = (1/\beta)\sum_n \hat{G}(\mathbf{k},\omega_n)e^{-i\omega_n\tau}$, we can get $-i\omega_n\hat{G}(\mathbf{k},\omega_n) = -\tau_z - \tau_z(H_{\mathbf{k}}+\Sigma_{\mathbf{k}})\hat{G}(\mathbf{k},\omega_n)$. Thus,

$$[i\omega_n - \tau_z(H_{\mathbf{k}}+\Sigma_{\mathbf{k}})]\hat{G}(\mathbf{k},\omega_n) = \tau_z.$$

By multiplying by the τ_z term on both sides, we can get the Dyson's equation in the main text.

From the diagonalization matrix $\Lambda_{\mathbf{k}}$, we have the relations $a_{\mathbf{k}} = u_{\mathbf{k},a,\alpha}\alpha_{\mathbf{k}} + u_{\mathbf{k},a,\beta}\beta_{\mathbf{k}} + v_{-\mathbf{k},a,\alpha}\alpha^\dagger_{-\mathbf{k}} + v_{-\mathbf{k},a,\beta}\beta^\dagger_{-\mathbf{k}}$ and $b_{\mathbf{k}} = u_{\mathbf{k},b,\alpha}\alpha_{\mathbf{k}} + u_{\mathbf{k},b,\beta}\beta_{\mathbf{k}} + v_{-\mathbf{k},b,\alpha}\alpha^\dagger_{-\mathbf{k}} + v_{-\mathbf{k},b,\beta}\beta^\dagger_{-\mathbf{k}}$. We here calculate the simplest term, $\Sigma^{12}_{\mathbf{k}}$, to show how to get the relation in Eq. (5). As $\Sigma^{12}_{\mathbf{k}} = -\frac{J_a g_{\mathbf{k}}}{2}\frac{1}{N}\sum_{\mathbf{q}}(\langle a^\dagger_{\mathbf{q}}a_{\mathbf{q}}\rangle + \langle b^\dagger_{\mathbf{q}}b_{\mathbf{q}}\rangle)$, using the relation above, we have

$$\begin{aligned}\sum_{\mathbf{q}}\langle a^\dagger_{\mathbf{q}}a_{\mathbf{q}}\rangle &= \frac{1}{N}\sum_{\mathbf{q}}(|u_{\mathbf{q},a,\alpha}|^2\langle\alpha^\dagger_{\mathbf{q}}\alpha_{\mathbf{q}}\rangle + |u_{\mathbf{q},a,\beta}|^2\langle\beta^\dagger_{\mathbf{q}}\beta_{\mathbf{q}}\rangle \\ &\quad + |v_{-\mathbf{q},a,\alpha}|^2\langle\alpha_{-\mathbf{q}}\alpha^\dagger_{-\mathbf{q}}\rangle + |v_{-\mathbf{q},a,\beta}|^2\langle\beta_{-\mathbf{q}}\beta^\dagger_{-\mathbf{q}}\rangle) \\ &= \sum_{\mathbf{q}}[|u_{\mathbf{q},a,\alpha}|^2 n_{\mathbf{q},\alpha} + |u_{\mathbf{q},a,\beta}|^2 n_{\mathbf{q},\beta} \\ &\quad + |v_{-\mathbf{q},a,\alpha}|^2(1+n_{-\mathbf{q},\alpha}) + |v_{-\mathbf{q},a,\beta}|^2(1+n_{-\mathbf{q},\beta}] \\ &= \sum_{\mathbf{q},\lambda=\alpha,\beta}(|u_{\mathbf{q},a,\lambda}|^2 + |v_{\mathbf{q},a,\lambda}|^2)n_{\mathbf{q},\lambda} + |v_{\mathbf{q},a,\lambda}|^2\end{aligned}$$

and

$$\sum_{\mathbf{q}}\langle b^\dagger_{\mathbf{q}}b_{\mathbf{q}}\rangle = \sum_{\mathbf{q},\lambda=\alpha,\beta}(|u_{\mathbf{q},b,\lambda}|^2 + |v_{\mathbf{q},b,\lambda}|^2)n_{\mathbf{q},\lambda} + |v_{\mathbf{q},b,\lambda}|^2.$$

So we have

$$\begin{aligned}\Sigma^{12}_{\mathbf{k}} &= -\frac{1}{N}\sum_{\mathbf{q},\lambda=\alpha,\beta}\sum_{\xi=a,b}\frac{J_a g_{\mathbf{k}}}{2}[(|u_{\mathbf{q},\xi,\lambda}|^2 + |v_{\mathbf{q},\xi,\lambda}|^2)n_{\mathbf{q},\lambda} \\ &\quad + |v_{\mathbf{q},\xi,\lambda}|^2].\end{aligned}$$

Comparing the equation above to Eq. (5), we can set $T^{\lambda}_{12}(\mathbf{k},\mathbf{q}) = -\frac{J_a g_{\mathbf{k}}}{2}\sum_{\xi=a,b}(|u_{\mathbf{q},\xi,\lambda}|^2 + |v_{\mathbf{q},\xi,\lambda}|^2)$ and $Q^{\lambda}_{12}(\mathbf{k},\mathbf{q}) = -\frac{J_a g_{\mathbf{k}}}{2}\sum_{\xi=a,b}|v_{\mathbf{q},\xi,\lambda}|^2$. The other elements of the self-energies can also be obtained using the same method above; then we can get the expression in Eq. (5) in the main text.

APPENDIX B: TEMPERATURE-INDUCED WEAK FERRIMAGNETIC PHASE

Due to sublattice asymmetries, the band degeneracies are broken. At finite temperatures, the occupation numbers for the two bands are different, $n_{\mathbf{q},\alpha} > n_{\mathbf{q},\beta}$. This will induce a weak ferrimagnetic phase. The total magnetization along the z direction is defined as $\langle S_z\rangle = \bar{S}_A - \bar{S}_B = \frac{1}{N}\sum_{\mathbf{k}}\langle b^\dagger_{\mathbf{k}}b_{\mathbf{k}}\rangle - \langle a^\dagger_{\mathbf{k}}a_{\mathbf{k}}\rangle$. From Fig. 6(a), we can see $\langle S_z\rangle$ does not equal zero at relatively high temperatures. The

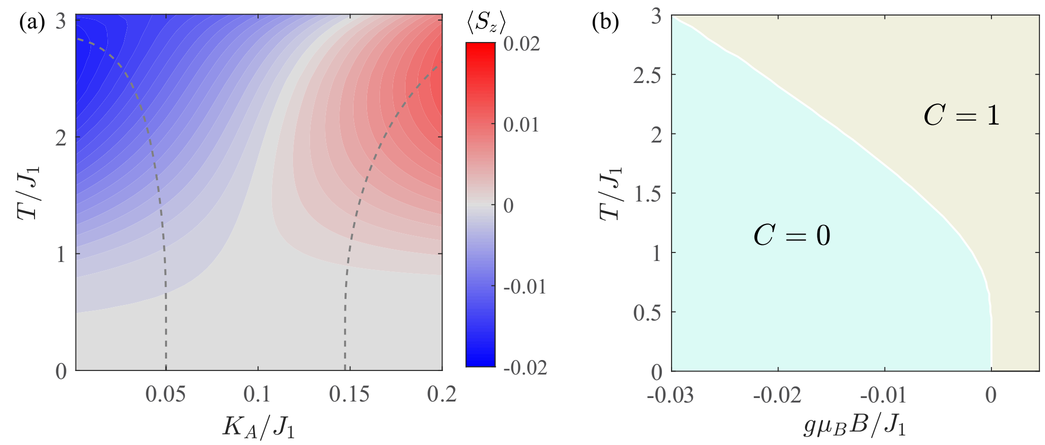

FIG. 6. (a) The total magnetization $\langle S_z\rangle$ distribution in the K_A-T plane. The dashed gray lines are the phase boundaries adopted from Fig. 3(a). (b) Phase diagram under magnetic field. $K_A = K_B = 0.05$. The other parameters are the same as in the main text.

two bands touching at the Γ point should satisfy the condition $K_A(-2S-1+4\bar{S}_A)+3(J_1+I_1)\bar{S}_B = K_B(-2S-1+4\bar{S}_B)+3(J_1+I_1)\bar{S}_A$. When $K_A = K_B$ and neglecting the MMIs, $\langle S_z\rangle = 0$, the two magnon bands are always degenerate at the Γ point, although $J_2^A \neq J_2^B$. But at finite temperature, $\langle S_z\rangle \neq 0$, the zero band gap condition at the Γ point is satisfied for a certain value of K_A with $K_A < K_B$, giving rise to the topological transitions at finite temperatures in the main text.

APPENDIX C: PHASE DIAGRAM UNDER A WEAK MAGNETIC FIELD

A weak perpendicular magnetic field can replace the role of easy-axis anisotropy asymmetry according to the above analysis for the band gap closing condition at the Γ point in the BZ. We set $K_A = K_B$ to verify this. The phase diagram is shown in Fig. 6(b). At zero temperature, a positive magnetic field gives a nontrivial topological phase for magnetic field, while a negative one gives a trivial phase. Across a magnetic-field-dependent critical temperature, the trivial phase can also go into the nontrivial phase.

APPENDIX D: THE DIPOLAR FIELD AND BOND-DEPENDENT INTERACTION

The role of the bond-dependent term can be replaced by the nearest-neighbor dipolar field. The dipole-dipole interaction (DDI) between two local spins is given by

$$H_{\mathrm{DDI}} = \frac{\mu_0(g\mu_B)^2}{2}\frac{\mathbf{S}_k\cdot\mathbf{S}_l - 3(\mathbf{S}_k\cdot\mathbf{e}_{kl})(\mathbf{S}_l\cdot\mathbf{e}_{kl})}{r_{kl}^3}.$$

$\mathbf{e}_{kl} = \mathbf{r}_{kl}/r_{kl} = (\cos\theta_{kl}, \sin\theta_{kl})$ is the unit vector pointing from site k to site l, and θ_{kl} is the bond angle with respect to the x axis. The first term in the numerator can be absorbed into the Heisenberg exchange interaction. The second term is bond dependent, $(\mathbf{S}_k\cdot\mathbf{e}_{kl})(\mathbf{S}_l\cdot\mathbf{e}_{kl}) = \frac{1}{4}(S_k^+e^{-i\theta_{kl}} + S_k^-e^{-i\theta_{kl}})(S_l^+e^{-i\theta_{kl}} + S_l^-e^{-i\theta_{kl}})$. With the relation $S^\pm = S^x \pm iS^y$, we have

$$\begin{aligned}(\mathbf{S}_k\cdot\mathbf{e}_{kl})&(\mathbf{S}_l\cdot\mathbf{e}_{kl})\\ &= \tfrac{1}{4}(S_k^+S_l^+e^{-2i\theta_{kl}} + S_k^-S_l^-e^{2i\theta_{kl}} + S_k^-S_l^+ + S_k^+S_l^-).\end{aligned}$$

As $\mathbf{S}_k\cdot\mathbf{S}_l = \frac{1}{2}(S_k^-S_l^+ + S_k^+S_l^-) + S_k^zS_l^z$, the last two terms in the parentheses can be absorbed into the Heisenberg exchange interaction but give an exchange anisotropy between the in-plane and out-of-plane directions. For the first two terms, the bond angle θ_{kl} for the three nearest-neighbor bonds are $-\pi/2$, $\pi/6$, and $5\pi/6$. For the $S_k^+S_l^+e^{-2i\theta_{kl}}$ term, the phase factors for the three bonds are -1, $-e^{i\frac{2\pi}{3}}$, and $-e^{i\frac{4\pi}{3}}$. Considering the minus sign of the bond-dependent term in H_{DDI}, we can get the formalism of the bond-dependent term in Eq. (1).

In our model, the sublattice asymmetries and the bond-dependent term are crucial for our results. The introduction of sublattice asymmetries is independent of the lattice type for collinear antiferromagnets. The bond-dependent term can be replaced by the dipolar interaction in other systems. Therefore, our proposal should be quite universal for the collinear antiferromagnets.

[1] M. Z. Hasan and C. L. Kane, Colloquium: Topological insulators, Rev. Mod. Phys. **82**, 3045 (2010).
[2] X.-L. Qi and S.-C. Zhang, Topological insulators and superconductors, Rev. Mod. Phys. **83**, 1057 (2011).
[3] N. P. Armitage, E. J. Mele, and A. Vishwanath, Weyl and Dirac semimetals in three-dimensional solids, Rev. Mod. Phys. **90**, 015001 (2018).
[4] B. A. Bernevig, T. L. Hughes, and S.-C. Zhang, Quantum spin hall effect and topological phase transition in HgTe quantum wells, Science **314**, 1757 (2006).
[5] M. S. Miao, Q. Yan, C. G. Van de Walle, W.-K. Lou, L. L. Li, and Kai Chang, Polarization-Driven Topological Insulator Transition in a GaN/InN/GaN Quantum Well, Phys. Rev. Lett. **109**, 186803 (2012).

[6] D. Zhang, W. K. Lou, M. S. Miao, S. C. Zhang, and K. Chang, Interface-Induced Topological Insulator Transition in GaAs/Ge/GaAs Quantum Wells, Phys. Rev. Lett. **111**, 156402 (2013).

[7] S.-Y. Xu, Y. Xia, L. A. Wray, S. Jia, F. Meier, J. H. Dil, J. Osterwalder, B. Slomski, A. Bansil, H. Lin, R. J. Cava, and M. Z. Hasan, Topological phase transition and texture inversion in a tunable topological insulator, Science **332**, 560 (2011).

[8] P. Dziawa, B. J. Kowalski, K. Dybko, R. Buczko, A. Szczerbakow, M. Szot, E. Łusakowska, T. Balasubramanian, B. M. Wojek, M. H. Berntsen, O. Tjernberg, and T. Story, Topological crystalline insulator states in $Pb_{1-x}Sn_xSe$, Nat. Mater. **11**, 1023 (2012).

[9] F. Zhao, T. Cao, and S. G. Louie, Topological Phases in Graphene Nanoribbons Tuned by Electric Fields, Phys. Rev. Lett. **127**, 166401 (2021).

[10] I. Garate, Phonon-Induced Topological Transitions and Crossovers in Dirac Materials, Phys. Rev. Lett. **110**, 046402 (2013).

[11] B. M. Wojek, M. H. Berntsen, V. Jonsson, A. Szczerbakow, P. Dziawa, B. J. Kowalski, T. Story, and O. Tjernberg, Direct observation and temperature control of the surface Dirac gap in a topological crystalline insulator, Nat. Commun. **6**, 8463 (2015).

[12] G. Antonius and S. G. Louie, Temperature-Induced Topological Phase Transitions: Promoted versus Suppressed Nontrivial Topology, Phys. Rev. Lett. **117**, 246401 (2016).

[13] T. Imai, J. Chen, K. Kato, K. Kuroda, T. Matsuda, A. Kimura, K. Miyamoto, S. V. Eremeev, and T. Okuda, Experimental verification of a temperature-induced topological phase transition in $TlBiS_2$ and $TlBiSe_2$, Phys. Rev. B **102**, 125151 (2020).

[14] P. Aguado-Puente and P. Chudzinski, Thermal topological phase transition in SnTe from *ab initio* calculations, Phys. Rev. B **106**, L081103 (2022).

[15] L. Lu, J. D. Joannopoulos, and M. Soljačić, Topological photonics, Nat. Photonics **8**, 821 (2014).

[16] J. Lu, C. Qiu, L. Ye, X. Fan, M. Ke, F. Zhang, and Z. Liu, Observation of topological valley transport of sound in sonic crystals, Nat. Phys. **13**, 369 (2017).

[17] R. Shindou, R. Matsumoto, S. Murakami, and J. Ohe, Topological chiral magnonic edge mode in a magnonic crystal, Phys. Rev. B **87**, 174427 (2013).

[18] Y.-M. Li, J. Xiao, and K. Chang, Topological magnon modes in patterned ferrimagnetic insulator thin films, Nano Lett. **18**, 3032 (2018).

[19] Z. Hu, L. Fu, and L. Liu, Tunable Magnonic Chern Bands and Chiral Spin Currents in Magnetic Multilayers, Phys. Rev. Lett. **128**, 217201 (2022).

[20] L. Zhang, J. Ren, J.-S. Wang, and B. Li, Topological magnon insulator in insulating ferromagnet, Phys. Rev. B **87**, 144101 (2013).

[21] A. Mook, J. Henk, and I. Mertig, Edge states in topological magnon insulators, Phys. Rev. B **90**, 024412 (2014).

[22] R. Chisnell, J. S. Helton, D. E. Freedman, D. K. Singh, R. I. Bewley, D. G. Nocera, and Y. S. Lee, Topological Magnon Bands in a Kagome Lattice Ferromagnet, Phys. Rev. Lett. **115**, 147201 (2015).

[23] S. K. Kim, H. Ochoa, R. Zarzuela, and Y. Tserkovnyak, Realization of the Haldane-Kane-Mele Model in a System of Localized Spins, Phys. Rev. Lett. **117**, 227201 (2016).

[24] T. Hirosawa, S. A. Díaz, J. Klinovaja, and D. Loss, Magnonic Quadrupole Topological Insulator in Antiskyrmion Crystals, Phys. Rev. Lett. **125**, 207204 (2020).

[25] H. Kondo and Y. Akagi, Dirac Surface States in Magnonic Analogs of Topological Crystalline Insulators, Phys. Rev. Lett. **127**, 177201 (2021).

[26] X. S. Wang, H. W. Zhang, and X. R. Wang, Topological Magnonics: A Paradigm for Spin-Wave Manipulation and Device Design, Phys. Rev. Appl. **9**, 024029 (2018).

[27] Y.-M. Li, Y.-J. Wu, X.-W. Luo, Y. Huang, and K. Chang, Higher-order topological phases of magnons protected by magnetic crystalline symmetries, Phys. Rev. B **106**, 054403 (2022).

[28] Y.-S. Lu, J.-L. Li, and C.-T. Wu, Topological Phase Transitions of Dirac Magnons in Honeycomb Ferromagnets, Phys. Rev. Lett. **127**, 217202 (2021).

[29] A. Mook, K. Plekhanov, J. Klinovaja, and D. Loss, Interaction-Stabilized Topological Magnon Insulator in Ferromagnets, Phys. Rev. X **11**, 021061 (2021).

[30] A. V. Chumak, V. I. Vasyuchka, A. A. Serga, and B. Hillebrands, Magnon spintronics, Nat. Phys. **11**, 453 (2015).

[31] V. Baltz, A. Manchon, M. Tsoi, T. Moriyama, T. Ono, and Y. Tserkovnyak, Antiferromagnetic spintronics, Rev. Mod. Phys. **90**, 015005 (2018).

[32] F. J. Dyson, General theory of spin-wave interactions, Phys. Rev. **102**, 1217 (1956).

[33] T. Oguchi, Theory of spin-wave interactions in ferro- and antiferromagnetism, Phys. Rev. **117**, 117 (1960).

[34] S. H. Liu, Nonlinear spin-wave theory for antiferromagnets, Phys. Rev. **142**, 267 (1966).

[35] B.-G. Liu, A non-linear spin-wave theory of quasi-2D quantum Heisenberg antiferromagnets, J. Phys.: Condens. Matter **4**, 8339 (1992).

[36] S. S. Pershoguba, S. Banerjee, J. C. Lashley, J. Park, H. Ågren, G. Aeppli, and A. V. Balatsky, Dirac Magnons in Honeycomb Ferromagnets, Phys. Rev. X **8**, 011010 (2018).

[37] Z. Li, T. Cao, and S. G. Louie, Two-dimensional ferromagnetism in few-layer van der Waals crystals: Renormalized spin-wave theory and calculations, J. Magn. Magn. Mater. **463**, 28 (2018).

[38] B. Wei, J.-J. Zhu, Y. Song, and K. Chang, Renormalization of gapped magnon excitation in monolayer $MnBi_2Te_4$ by magnon-magnon interaction, Phys. Rev. B **104**, 174436 (2021).

[39] V. V. Mkhitaryan and L. Ke, Self-consistently renormalized spin-wave theory of layered ferromagnets on the honeycomb lattice, Phys. Rev. B **104**, 064435 (2021).

[40] A. Mook, S. A. Díaz, J. Klinovaja, and D. Loss, Chiral hinge magnons in second-order topological magnon insulators, Phys. Rev. B **104**, 024406 (2021).

[41] T. Matsumoto and S. Hayami, Nonreciprocal magnons due to symmetric anisotropic exchange interaction in honeycomb antiferromagnets, Phys. Rev. B **101**, 224419 (2020).

[42] T. J. Hicks, T. Keller, and A. R. Wildes, Magnetic dipole splitting of magnon bands in a two dimensional antiferromagnet, J. Magn. Magn. Mater. **474**, 512 (2019).

[43] R. Hidalgo-Sacoto, R. I. Gonzalez, E. E. Vogel, S. Allende, J. D. Mella, C. Cardenas, R. E. Troncoso, and F. Munoz, Magnon valley Hall effect in CrI_3-based van der Waals heterostructures, Phys. Rev. B **101**, 205425 (2020).

[44] F. Xiao and Q. Tong, Tunable strong magnetic anisotropy in two-dimensional van der Waals antiferromagnets, Nano Lett. **22**, 3946 (2022).
[45] J. B. Fouet, P. Sindzingre, and C. Lhuillier, An investigation of the quantum $J_1 - J_2 - J_3$ model on the honeycomb lattice, Eur. Phys. J. B **20**, 241 (2001).
[46] K. H. Lee, S. B. Chung, K. Park, and J.-G. Park, Magnonic quantum spin Hall state in the zigzag and stripe phases of the antiferromagnetic honeycomb lattice, Phys. Rev. B **97**, 180401(R) (2018).
[47] A. L. Fetter and J. D. Walecka, *Quantum Theory of Many-Particle Systems*, Dover Books on Physics (McGraw-Hill, New York, 2003).
[48] J. Li, R.-L. Chu, J. K. Jain, and S.-Q. Shen, Topological Anderson Insulator, Phys. Rev. Lett. **102**, 136806 (2009).
[49] S. Stützer, Y. Plotnik, Y. Lumer, P. Titum, N. H. Lindner, M. Segev, M. C. Rechtsman, and A. Szameit, Photonic topological Anderson insulators, Nature (London) **560**, 461 (2018).
[50] E. J. Meier, F. A. An, A. Dauphin, M. Maffei, P. Massignan, T. L. Hughes, and B. Gadway, Observation of the topological Anderson insulator in disordered atomic wires, Science **362**, 929 (2018).
[51] X.-W. Luo and C. Zhang, Photonic topological insulators induced by non-Hermitian disorders in a coupled-cavity array, arXiv:1912.10652.
[52] S. M. Rezende, A. Azevedo, and R. L. Rodríguez-Suárez, Introduction to antiferromagnetic magnons, J. Appl. Phys. **126**, 151101 (2019).
[53] J. Cenker, B. Huang, N. Suri, P. Thijssen, A. Miller, T. Song, T. Taniguchi, K. Watanabe, M. A. McGuire, D. Xiao, and X. Xu, Direct observation of two-dimensional magnons in atomically thin CrI_3, Nat. Phys. **17**, 20 (2021).
[54] Y. Nambu, J. Barker, Y. Okino, T. Kikkawa, Y. Shiomi, M. Enderle, T. Weber, B. Winn, M. Graves-Brook, J. M. Tranquada, T. Ziman, M. Fujita, G. E. W. Bauer, E. Saitoh, and K. Kakurai, Observation of Magnon Polarization, Phys. Rev. Lett. **125**, 027201 (2020).
[55] Y. Liu, Z. Xu, L. Liu, K. Zhang, Y. Meng, Y. Sun, P. Gao, H.-W. Zhao, Q. Niu, and J. Li, Switching magnon chirality in artificial ferrimagnet, Nat. Commun. **13**, 1264 (2022).
[56] Y. Shiota, T. Arakawa, R. Hisatomi, T. Moriyama, and T. Ono, Polarization-Selective Excitation of Antiferromagnetic Resonance in Perpendicularly Magnetized Synthetic Antiferromagnets, Phys. Rev. Appl. **18**, 014032 (2022).
[57] T. Arakawa, Y. Shiota, K. Yamada, T. Ono, and S. Kon, Magnetic polarization selective spectroscopy of magnetic thin films probed by wideband crossed microstrip circuit in GHz regime, Rev. Sci. Instrum. **93**, 013901 (2022).
[58] H. Katsura, N. Nagaosa, and P. A. Lee, Theory of the Thermal Hall Effect in Quantum Magnets, Phys. Rev. Lett. **104**, 066403 (2010).
[59] R. Matsumoto and S. Murakami, Theoretical Prediction of a Rotating Magnon Wave Packet in Ferromagnets, Phys. Rev. Lett. **106**, 197202 (2011).
[60] A. R. Wildes, B. Roessli, B. Lebech, and K. W. Godfrey, Spin waves and the critical behaviour of the magnetization in $MnPS_3$, J. Phys.: Condens. Matter **10**, 6417 (1998).
[61] B. L. Chittari, Y. Park, D. Lee, M. Han, A. H. MacDonald, E. Hwang, and J. Jung, Electronic and magnetic properties of single-layer MPX_3 metal phosphorous trichalcogenides, Phys. Rev. B **94**, 184428 (2016).
[62] S. Calder, A. V. Haglund, A. I. Kolesnikov, and D. Mandrus, Magnetic exchange interactions in the van der Waals layered antiferromagnet $MnPSe_3$, Phys. Rev. B **103**, 024414 (2021).
[63] M. Mi, X. Zheng, S. Wang, Y. Zhou, L. Yu, H. Xiao, H. Song, B. Shen, F. Li, L. Bai, Y. Chen, S. Wang, X. Liu, and Y. Wang, Variation between antiferromagnetism and ferrimagnetism in $NiPS_3$ by electron doping, Adv. Funct. Mater. **32**, 2112750 (2022).